THESIS

DYNAMICS OF CONVECTIVE ORGANIZATION IN AFRICAN EASTERLY WAVES OBSERVED DURING THE NAMMA AND CPEX-CV FIELD CAMPAIGNS

Submitted by

Delián Colón-Burgos

Department of Atmospheric Science

In partial fulfillment of the requirements

For the Degree of Master of Science

Colorado State University

Fort Collins, Colorado

Summer 2025

Master's Committee

Advisor: Michael M. Bell

Eric Maloney
Frances Davenport

ABSTRACT

DYNAMICS OF CONVECTIVE ORGANIZATION IN AFRICAN EASTERLY WAVES OBSERVED DURING THE NAMMA AND CPEX-CV FIELD CAMPAIGNS

The mechanisms that govern the organization of moist convection in weakly rotating flows such as tropical easterly waves are not fully understood. In this study we aim to better understand the dynamical processes that govern the convective organization at the meso-alpha scale, including the location, and intensity of deep convection, using NASA airborne field campaign and satellite observations. We employ a 3D variational analysis technique called SAMURAI in a vortex-centric approach, integrating ERA5 reanalysis and research aircraft observations of 20 African easterly wave (AEW) cases collected during NAMMA in 2006 and CPEX-CV in 2022. The SAMURAI analyses are centered on a potential vorticity (PV) centroid and show a low-level wave relative circulation across cases. Convection is classified from satellite imagery into three classes of shallow/moderate and deep to obtain a frequency of the occurrence relative to the PV centroid location. We find four clusters of organized deep convection denoted as minimal deep, southern, southwestern, and widespread, with the southwestern and widespread clusters associated with the greatest magnitudes of frequency. Results from a composite analysis reveal high PV and relative humidity (RH) at mid-levels were approximately co-located with the regions of low-level convergence and more frequent deep convection, particularly for the southwestern and widespread clusters. Waves with a higher frequency of deep convection are characterized by stronger PV and higher RH at mid-levels compared to waves with a lower frequency of deep convection. Further research is recommended

to explore these relationships temporally to better determine the role of cause and effect between the PV and RH and deep convective organization.

ACKNOWLEDGEMENTS

I would like to acknowledge my research advisor Michael Bell and committee members Eric Maloney and Frances Davenport. I would also like to thank my family, friends, and members of the Bell group for their continuous support.

This research was supported by the NASA grant #80NSSC23K1306 under the Weather and Dynamics Focus Area. We acknowledge the science teams of the NAMMA and CPEX-CV NASA field experiments and the dropsonde quality control efforts of NCAR/EOL.

TABLE OF CONTENTS

CHAPTER 1- Introduction

African easterly waves (AEWs) are a weakly rotating tropical feature that originate over Africa and propagate westward across the Atlantic Ocean. AEWs are mostly known for being the precursors to hurricanes (Avila and Pash, 1992; Landsea et al. 1993), being the origin of approximately 60% of Atlantic tropical cyclones and of approximately 85% of intense Atlantic hurricanes (NOAA AOML). About 20% of objectively tracked AEWs served as tropical cyclone (TC) precursors during July-October 1984-2009 (Enyew & Mekonnen, 2022). Knowing which weakly rotating features will ultimately develop into a TC still remains a significant forecast problem. AEWs also modulate the rainfall over West Africa (Reed et al., 1977), helping explain more than 40% of the total convective variance over the eastern Atlantic during boreal summer (Mekonnen et al., 2006). Given their transatlantic propagation these are significant contributors to precipitation in communities across the Caribbean and South America. AEWs contribute 30–50% of the total precipitation over northern South America and the Caribbean Sea and up to 60% over Central America during boreal summer (Poveda et al., 2002; Dominguez et al., 2020). Therefore, understanding the ingredients and dynamics of these organized convective systems, regardless of whether they undergo cyclogenesis, is essential.

Earlier studies suggested that AEW development occurs primarily through baroclinic instability to the African Easterly Jet (AEJ) (Burpee, 1972; Reed et al., 1988). More recent research has indicated that the linear instability of the AEJ alone doesn't explain the growth and maintenance of AEWs (Hall et al., 2006; Hsieh & Cook, 2005; Russell et al., 2020). Multiple studies have found a dual character in the wave formation location, happening in two different latitude belts (Reed at al., 1988; Pytharoulis and Thorncroft, 1999; Thorncroft & Hodges, 2001).

A northern belt around 22°N overlapping with the African monsoon trough north of the AEJ, and a southern belt around 12°N closer to the Intertropical Convergence Zone (ITCZ). Southern track waves have been associated with stronger and deeper convection than the weak and more shallow convection found in the northern track waves (Pytharoulis and Thorncroft, 1999). Although baroclinic instability was found to be mainly responsible for the maintenance and development of AEWs in the northern track, convection is particularly important for the southern track waves, which have shown to have a greater conversion rate to TCs than northern track AEWs (Chen et al. 2008). Recent modeling studies found that contributions to growth by barotropic and baroclinic instability were relatively small in comparison to those due to convective heating (Hall et al., 2006; and Russell and Aiyyer, 2019; Russel et al., 2020; Adames, 2022). This suggests the exploration of the characteristics, location and intensity of convection within AEWs is particularly important for understanding their evolution and development.

Significant differences in strength and location of convection have been found when comparing between developing and non-developing disturbances for cyclogenesis (Hopsh et al., 2009; Agudelo 2011, Kim et al. 2025). Deep organized convection in non-developing waves tends to be weaker than in developing wave composites (Enyew and Mekonnen, 2022), but multiple studies (Leppert et al. 2013, Zawislak and Zipser 2014, Núñez Ocasio et al. 2020) have shown the areal coverage of convection to be a better indicator of cyclogenesis rather than the overall intensity of convection. In addition to increased convection, the large-scale moisture and upper-level divergence were found to be among the most important parameters for distinguishing between developing and non-developing AEWs (Leppert et al. 2013). Various studies (Brammer and Thorncroft, 2015; Hopsch et al., 2010; Enyew and Mekonnen, 2022) have emphasized the

importance of the presence of moisture to support convection and development of AEWs, particularly ahead of the wave (Brammer et al. 2018). For example, Brammer and Thorncroft (2015) examined waves exiting West Africa and found that developing waves showed a higher tropospheric moisture content to the northwest of the trough that then gets ingested into lower levels, favoring development. Studies have also highlighted factors like synoptic-scale ascent and wind shear playing an important role in the AEW-convection interactions (Janiga & Thorncroft, 2016; Kiladis et al., 2006).

The location of the mesoscale convective systems (MCSs) relative to the AEW trough has also been hypothesized to be an important factor in feeding further development of the wave. A composite analysis of developing waves revealed well-organized MCSs to be coupled and collocated with the AEW trough over oceans (Hopsch et al. 2010; Enyew and Mekonnen, 2022). This coupling of deep convection to the AEW trough was also highlighted as an important piece for development in an analysis of the precursor of Hurricane Alberto (Lin et al., 2005) and further investigated in Núñez Ocasio et al. (2020). After tracking MCSs in AEWs and examining their propagation in a wave-relative framework, they found that convection in developing waves is latitudinally coupled and in phase with the wave trough, which aids in further intensification through latent heat release induced by potential vorticity generation (Núñez Ocasio et al., 2020). Conversely, in non-developing waves, convection was found further south of the wave vortex, which tends to outrun the wave. Clearly, convection has been shown to be an essential factor for the strengthening of waves, but the dynamics of the processes involved is still a subject of ongoing research.

The generation of vorticity anomalies in MCSs (Schubert et al. 1991, Schwendike and Jones (2010), Bell and Montgomery (2019)) have been analyzed as an important factor

facilitating a positive feedback process for strengthening of an AEW. Schwendike and Jones (2010) found that the vertical alignment of a mid-level anomaly produced by convection with the low-level circulation aided in the intensification of pre- Helene through vortex stretching. Similarly, Bell and Montgomery (2019) also found positive vortex stretching at the meso-alpha scale to be associated with convergence in the lower troposphere from deep convective heating in pre-depression Karl. The concept that convection driven vortex stretching can lead to strengthening was also discussed by Adames and Ming (2018) for synoptic-scale Asian monsoonal disturbances and Rydbech and Maloney (2015) for Pacific easterly waves. A conceptual framework of moist convective dynamics was proposed by Russell et al. 2020 from results of convective permitting simulations, where they suggest that positive low-level potential vorticity (PV) anomalies driven by diabatic heating from deep moist convection help maintain the column of PV associated with AEWs.

Although recent literature has highlighted the importance of convection at the mesoscale for maintenance and strengthening of AEWs, fundamental questions about where and when convection will occur still remain unanswered. While we understand many of the fundamental ingredients that lead to convective storms and heavy precipitation (Doswell et al., 1996), our understanding of the dynamics that organize convection within AEWs is still limited. Understanding moist convection in weak rotation environments over the tropical oceans is a particularly challenging regime, since conditions for convection are broadly favorable, but the spatial and temporal occurrence of convection is highly variable. Mesoscale observations in this region are sparse, and consequently many of the theories and hypothesis on AEWs are based on modeling or larger-scale reanalysis.

In this thesis we aim to analyze the characteristics and dynamics of deep convection in AEWs analyzing observations from two NASA field campaigns over the Eastern Atlantic using a PV focused, vortex-centric approach at the meso-alpha scale. Although a wave centric approach, which many previous studies have adopted, can be useful for studying synoptic scale evolution, we focus herein on the mesoscale organization for which a vortex-centric approach is appropriate. Additionally, studies like Russell et al. (2020) and Adames and Ming (2018) have demonstrated the value of investigating AEW development within a synoptic-scale PV framework since its non-conservation can be directly attributed to diabatic processes (Hoskins et al., 1985). Our research is guided by two research questions: (1) What are the convective characteristics of AEWs using a vortex-centric approach? and (2) How do moisture and potential vorticity relate to the convective organization in African easterly waves at the meso-alpha scale? Better understanding of the dynamics that govern the convective organization in AEWs can translate to improved prediction of rainfall associated with these systems and inform ongoing research in the cyclogenesis space.

CHAPTER 2- Data and Methods

2.1 Data

To examine the processes and ingredients that govern the convective organization in tropical weakly rotating flows, 20 cases of African easterly waves (AEWs) were identified. These cases correspond to research flights from two field campaigns, employing NASA's DC-8 flying laboratory in the tropical East Atlantic, between 42°W- 14° W and 2° N- 26° N. Eleven cases were chosen from the NASA African Monsoon Multidisciplinary Analysis (NAMMA) in 2006 and 9 from the Convective Processes Experiment- Cabo Verde (CPEX-CV) in 2022 (Fig. 1). Various AEW intensities and convection types are represented in the cases, ranging from scattered convection to more mature mesoscale convective systems (MCS).

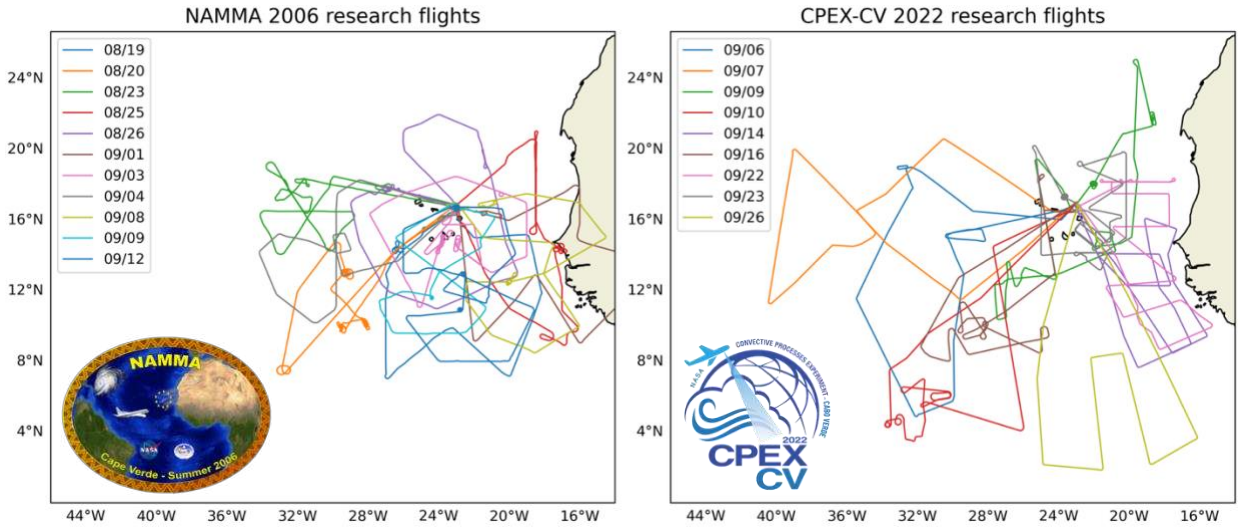

Figure 1. Research flight tracks of selected cases from the NAMMA (11 cases) and CPEX-CV (9 cases) field campaigns.

Table 1. Case characteristics, including coordinates of PV centroid at 1200 UTC, identified system number from the Q-track, derived wave motion and system name associated with development. In the cluster group column, 1= Minimal deep, 2= Southern, 3= Southwestern, and 4= Widespread.

Case date	PV centroid Longitude [°]	PV centroid Latitude [°]	System number in Q-track	U [m/s]	V [m/s]	System name if developer	Cluster group
2006-08-19	-27.25	9	36	-13.28	-1.09	ERNESTO	2
2006-08-20	-33.75	11.75	36	-11.57	-0.17	ERNESTO	2
2006-08-23	-32	17.25	37	-9.85	4.57	DEBBY	2
2006-08-25	-18	16	39	-7.85	2.42	-	2
2006-08-26	-24.5	16.75	39	-10.13	0.55	-	1
2006-09-01	-23.75	13.25	43	-14.8	-1.15	FLORENCE	2
2006-09-03	-22.25	15.75	41	-14.71	3.1	-	3
2006-09-04	-28.75	15	41	-6.58	0.63	-	3
2006-09-08	-18.5	14	48	-7.45	-0.94	-	3
2006-09-09	-23.5	16.5	48	-6.28	3.84	-	1
2006-09-12	-22	11.75	46	-10.39	-0.15	HELENE	4
2022-09-06	-27.75	14.5	49	-10.41	0.25	-	4
2022-09-07	-34.5	16.75	49	-9.39	1.75	-	4
2022-09-09	-26.5	9.5	51	-10.33	-2.47	FIONA	3
2022-09-10	-31.25	10.5	51	-8.28	4.34	FIONA	1
2022-09-14	-14.25	10.5	52	-15.11	3.77	IAN	4
2022-09-16	-27.75	10.25	52	-10.83	0.85	IAN	3
2022-09-22	-16	15.75	55	-7.84	3.79	HERMINE	3
2022-09-23	-20.5	18.75	55	-4.62	0.51	HERMINE	4
2022-09-30	-21.5	9.75	58	-5.7	0.35	-	2

The 20 cases analyzed feature various types of convection based on NAMMA and CPEX-CV mission reports, including MCSs, scattered convection, a range of intensities (some weaker waves and others closer to depression stage), and with an average translation speed of 10 m/s across cases. From the cases sampled, 11 were developing waves and 9 were non-developers (Table 1). The developing waves include Ernesto, Debby, Florence, Helene, Fiona, Ian, and Hermine. Given our small sample size, statistics on comparisons between developing and non-developing will not be discussed in this thesis. Non-developer waves were sampled around the

time of peak intensity, up to 60 hours from peak intensity, while most developing waves were mostly sampled days ahead of reaching their peak intensity in the Caribbean or Gulf. An exception to this were Hermine and Debby, which were sampled close to the time of peak intensity. Given the nature of the field campaign design and the translation speed of these waves, some cases are the same wave, just 24 hours after. These cases have the same system number identified from the Q-track database (Lawton et al. 2022) (Table 1). Eight pairs of cases are dependent, the same wave sampled twice, and 4 independent cases, which were just sampled once. Its important to recognize that this dependency may bring some bias to the analysis, or in the contrary, bring greater weight to our argument in some scenarios. In this thesis we will focus on examining the convective structure and the leading dynamic and thermodynamic factors, regardless of their development.

Both campaigns operated out of the Sal Island, Cabo Verde. The NAMMA field campaign took place during August 6 -September 10, 2006, and focused on characterizing the evolution and structure of AEWs and MCSs over continental western Africa, and their impacts on energy and water budgets (Snyder and Pu, 2010), incorporating both surface and aircraft observations. The CPEX-CV airborne field campaign studied tropical convection and associated processes affecting tropical North Atlantic dynamics (Zawislak et al., 2022) during September 2022. Various instruments onboard the DC-8 provided measurements of winds, temperature, water vapor, precipitation and tropospheric aerosols (Nowottnick et al., 2024). In this study we incorporate observations from a) dropsondes, which provide a vertical atmospheric profile of temperature, moisture, wind and pressure; b) along-track 2-μm measurements of horizontal wind speed from the Doppler aerosol wind (DAWN) lidar (Bedka et al. 2021; Greco et al. 2020a,b; Kavaya et al. 2014); c) temperature and water vapor passive observations from the High-Altitude

Monolithic Microwave Integrated Circuit (MMIC) Sounding Radiometer (HAMSR) (Brown et al. 2011); and d) in-situ flight level thermodynamic and dynamical observations from the DC-8.

2.2 SAMURAI Analysis

We employ the Spline Analysis at Mesoscale Utilizing Radar and Aircraft Instrumentation (SAMURAI) to integrate NASA's DC-8 observations with reanalysis (Fig. 2). SAMURAI is a unique 3D variational data assimilation and analysis package that can analyze 3D dynamic and thermodynamic fields from various data sources (Bell et al., 2012; Cha and Bell, 2023). The software allows analysis in a vortex-centric approach through a time-space correction of observations due to the movement of the wave.

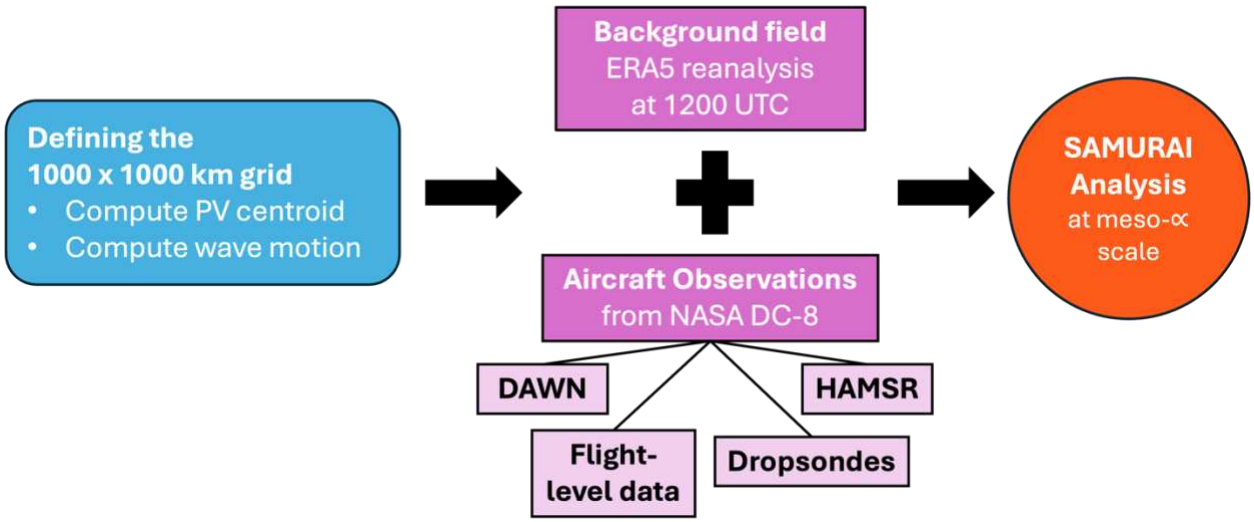

Figure 2. Schematic of methods on running SAMURAI, including the data incorporated.

SAMURAI takes as input a first guess background estimate, a moving frame of reference center location, and the observational data. For the background estimate, we use the fifth generation ECMWF reanalysis (ERA5) (Hersbach et al. 2023) which provides hourly estimates

of various dynamic and thermodynamic atmospheric variables at a 0.25° x 0.25° grid-spacing. The analysis then incorporates observations from instruments onboard the NASA DC-8 aircraft, including atmospheric observations from dropsondes, relative humidity measurements from HAMSR, and in-situ flight level, static temperature, and dew point temperature, were included for all cases. Winds measured by DAWN were also incorporated in the SAMURAI analyses for the nine CPEX-CV cases. We ran SAMURAI for a fixed time (1200 UTC), employing the 1200 UTC ERA5 Reanalysis but considering observations for the entirety of the flight period. The flight period varies per flight but all are between 0500- 2000 UTC. Sensitivity to using ERA5 from 0600 UTC and 1800 UTC as the estimate was tested and differences were small.

With the goal of performing the analysis in a "vortex centric" approach at the meso-alpha scale, a 1000 x 1000 km grid (± 500 km from the center) with 10 km horizontal grid spacing and 1 km vertical grid spacing was utilized. The 10-km grid spacing was used in order to represent features on the meso-alpha scale. To map the ERA5 ~25 km grid spacing estimate to the finer 10 km grid, a distance weighted interpolation was used in combination with a low-pass filter. A PV centroid was used as the "center" of the meso-alpha scale vortex within the synoptic scale wave for each case. The PV centroid maximizes the area integrated PV from ERA5 in the lower troposphere in a box extending ±3 degrees in each direction and between 850-500 hPa of altitude. From the area integrated PV grid, the point with the largest area integrated PV in a bounding box around the flight path, to avoid capturing other high PV features not associated with the wave, was designated as the PV centroid. The derived PV centroid coordinates for each case are shown in Table1.

The wave motion was derived by performing a fourth-order finite differencing from the wave track in Qtrack, an objective African Easterly Wave Track dataset from Reanalysis data

(Lawton et al. 2022) (Table 1). The Qtrack derives 6-hourly center points of AEWs by calculating the curvature vorticity using the nondivergent component of the 700-hPa ERA5 wind and then performing an average within 600 km radius in each grid point. The calculation was performed over 5 points using a fourth-order centered finite difference (Eq. 1) over 6 hours with the center point at 1200 UTC on the day of interest. We derived the wave speed from the Q-track, focused on the synoptic scale evolution, rather than deriving PV centroids every 6 hours since the centroid doesn't often follow the synoptic-scale east to west AEW translation, as it can reorganize and advect within the broader wave itself and be difficult to track.

$$(1)\ u_o = \frac{\partial x}{\partial t} = \frac{-x(t_o + 2\,\Delta t) + 8x(t_o + \Delta t) - 8x(t_o - \Delta t) + x(t_o - 2\,\Delta t)}{12\,\Delta t}$$

After running SAMURAI, vortex-centric 3D fields of various thermodynamic and dynamical variables are obtained. Figure 3 shows an example of the PV and relative humidity (RH) fields analyzed by SAMURAI for the 20220907 case, including the original ERA5 reanalysis, the background which is the ERA5 with an additional low-pass filter, the analysis, and the analysis increment which is the analysis minus the background estimate. Note that the location where the dropsondes were launched along the flight path match up with the differences in the increment file. Potential vorticity was computed at each level using the Metpy function to calculate baroclinic potential vorticity (Eq. 2) utilizing the potential temperature (θ), pressure (p), zonal velocity (u) and meridional velocity (v) from the SAMURAI analysis.

$$(2)\ PV = -g\left(\frac{\partial u}{\partial p}\frac{\partial \theta}{\partial y} - \frac{\partial v}{\partial p}\frac{\partial \theta}{\partial x} + \frac{\partial \theta}{\partial p}(\zeta + f)\right)$$

From Fig. 3 we can see how the SAMURAI analysis synthesizes the observations from the DC-8 aircraft with the ERA5 background estimate into 3D fields designed for analysis of AEW structure at the meso-alpha scale centered on the low-level PV centroid.

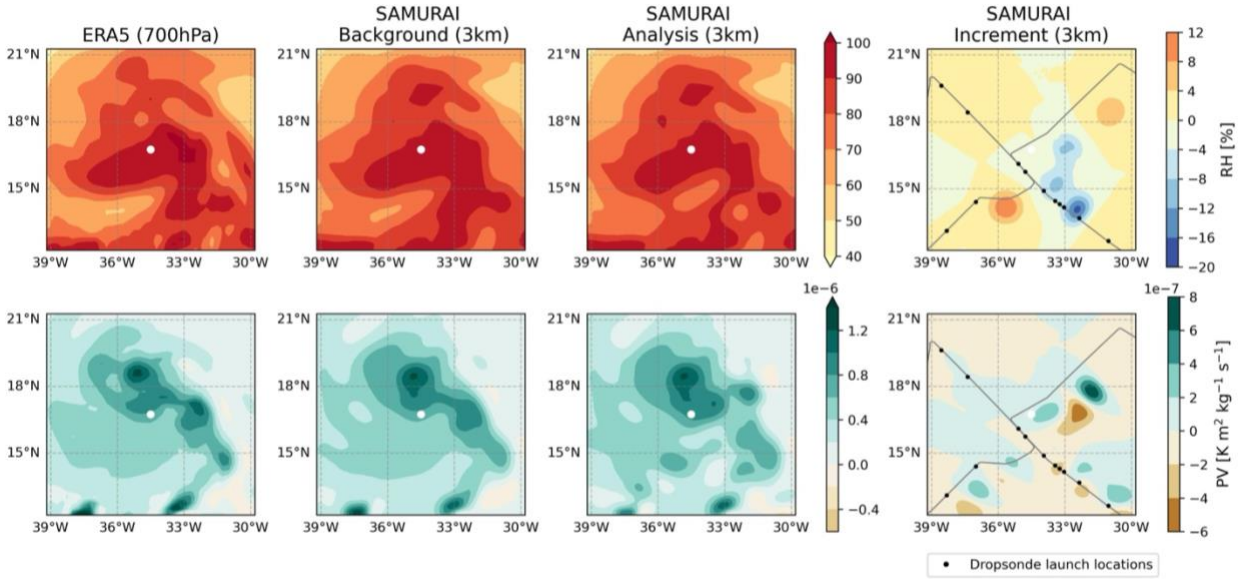

Figure 3. Comparison between ERA5 Reanalysis at 700hPa, SAMURAI background, analysis and increment at 3 km for relative humidity (RH) and potential vorticity (PV) during the 1200 UTC Sept 7, 2022 case. Fields shown are 1000 x 1000 km and centered on the derived PV centroid. Black dots show the dropsonde launch locations from the NASA DC8 aircraft during RF5 of the CPEX-CV field campaign.

2.3 Satellite Brightness Temperature Analysis

To analyze how the intensity and distribution of convection relates to the SAMURAI fields at multiple levels, convection is characterized from satellite infrared (IR) brightness temperatures. For CPEX-CV, we examine the GOES-16 ABI product channel 13 (CMI_C13) centralized at a wavelength of 10.3 μm, which has a 2 km spatial resolution and a 10-minute frequency. Data were obtained through the goes2go python package. For NAMMA cases NCEP/CPC L3 Half-Hourly 4 km merged IR (Janowiak et al., 2017) was employed, as ABI satellite technology was not available in 2006. This datum has a 4 km spatial resolution and a 30-minute temporal resolution.

IR images over a 6-hour window centered around 1200 UTC (0900 – 1500 UTC) were compiled for each case. These images have dimensions of 1000 x 1000 km (matching the SAMURAI grids) and are centered on the closest PV centroid corresponding to the time of the IR image. Given the difference in temporal resolution of the images between 2006 and 2022, there are 12 images for each NAMMA case and 36 images for each CPEX-CV case. We performed a nearest neighbor resampling with a radius of influence of 15 km, using pyresample, to get the brightness temperature fields to be the same resolution as the SAMURAI fields (10 km).

Convection is classified into clear sky, shallow/moderate and deep convection for each resampled image based on the brightness temperature values, using the definitions shown in Table 2. The values used in this study are similar to those used in Giangrande et al. (2017). Atmospheric temperature ranges corresponding to the heights for each convection classification were derived from the spatial and temporal average vertical profile across the 20 SAMURAI analyses. Then, the spatial frequency of each type of convection was calculated for each case by counting up the grid points that had a certain type of convection across the images over the 6 hours, and dividing by the total number of images (12 or 36 depending on the case year).

Table 2. Convection classification and associated cloud-top height and atmospheric temperature definitions.

Cloud Type	Cloud-top height [km]	Temperature [K]
Clear sky	< 0.5 km	T >293
Shallow/Moderate convection	0.5-8 km	$253 \leq T \leq 293$
Deep convection	> 8 km	T < 253

CHAPTER 3- Results

First, we describe the characteristics of the AEW cases being studied, and examine the spatial distribution and frequency of convection from brightness temperature images. Then based on identified patterns of frequency of deep convection, we analyze how the magnitude, spatial structure, and variability of PV and RH relate to where the deep convection was located.

3.1 Characterization of convection and clustering

To characterize the convection observed during the near-flight times in each case, the frequency of convection over 6 hours was computed from GOES satellite brightness temperatures. Figure 4 shows an example of the satellite brightness temperature images closest to 0900, 1200, and 1500 UTC, and the resulting frequency of clear air, shallow/moderate, and deep convection a certain pixel relative to the PV centroid had. For example, pixels that show a frequency of convection of 0.8-1 indicate that in 80-100% of the total of images over the 6 hours, that type of convection was present. The 20220906 case (Fig. 4) shows convection present across most of the domain between 0900- 1500 UTC, with just a small area of clear air in the left central region in the upper left quadrant, where no convection was identified over the 6 hours. Convection was characterized by a large frequency of deep convection extending from the SW to NE quadrant, first organized in three main convective areas evolving into a more linear structure, with 51.5% of the pixels in the southwest quadrant showing a frequency of deep convection of 0.8 or higher and 37.8% in the northeast quadrant.

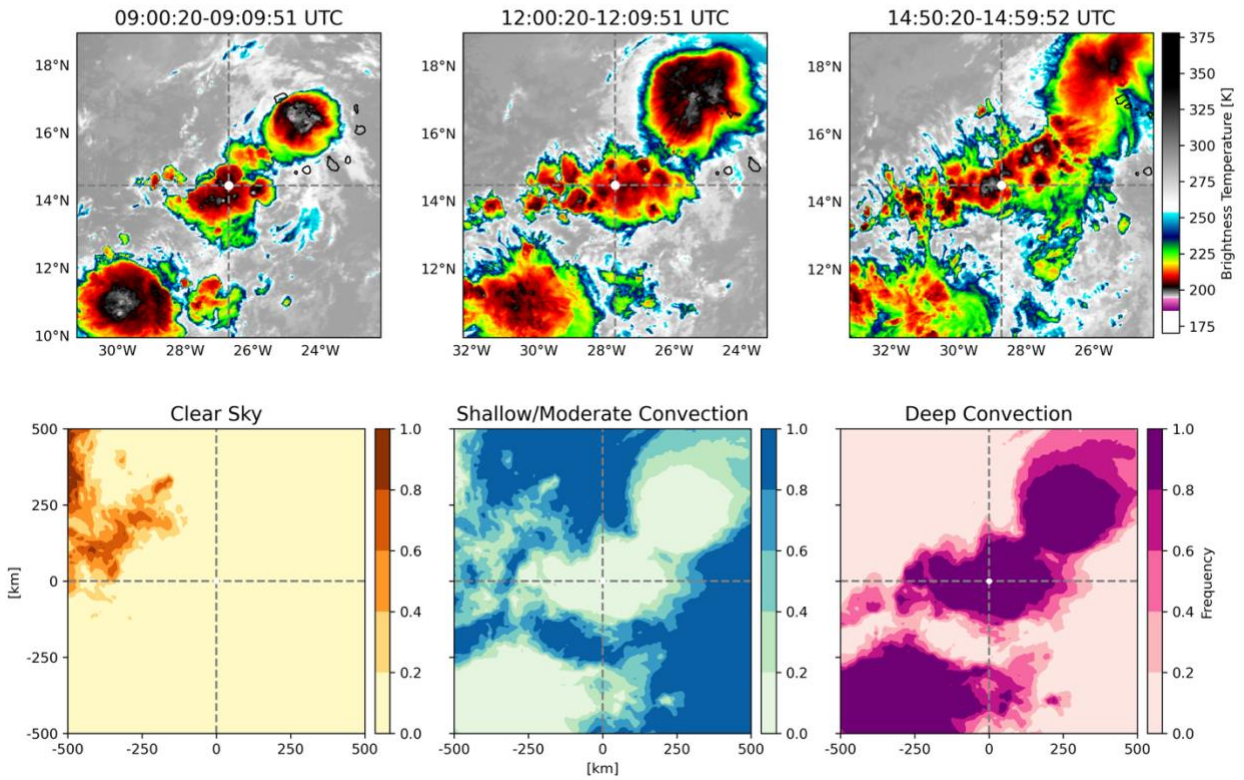

Figure 4. Infrared satellite images (1000 x 1000 km) during 0900, 1200 and 1500 UTC for the September 6, 2022 case, centered at the PV centroid during respective time (top). Frequency of clear sky, shallow/moderate convection and deep convection over 6 hours (0900 – 1500 UTC) is shown in the bottom row.

Figure 5 shows the frequency of deep convection for all cases and illustrates a variety of spatial patterns. Some cases, like 20220930 and 20220916, show a more scattered structure, while others, like 20060912 and 20220907, show a more organized structure. Even with the high variability, patterns of how this deep convection was distributed relative to the centroid are apparent by eye. Ultimately our goal is to better understand where the convection will occur, particularly deep convection for forecasting applications. Therefore we decided to cluster the cases by the spatial distribution of the frequency of deep convection, which aided in the characterization of the waves. We ran a k-means clustering algorithm to group cases with similar

spatial distributions of frequency of deep convection, testing for various values of k, including k=3, k=4, and k=5. Three clusters showed to be the appropriate amount, where spatial patterns of deep convection remained unique across clusters. The k-means identified deep convection south of the PV centroid (lower two quadrants), deep convection focused SW of the PV centroid (lower left quadrant), and deep convection with widespread coverage in the 1000 x 1000 km extent. From subjective examination, we identified 3 cases that showed minimal deep convection or was found away from the centroid. The addition of a classification of minimal deep convection enhanced the patterns of deep convection organization identified by k-means. Results from a k-means clustering algorithm and subjective modification, show 4 clusters of how the deep convection is organized relative to the PV centroid. Throughout the thesis we will refer to these classifications using the following language: cluster 1: “minimal deep” with N= 3, cluster 2: “south” with N= 6, cluster 3: “southwestern” with N= 6, and cluster 4: “widespread” with N=5. Note that three of the pairs of same waves (Table 1) were classified under the same cluster (2006-08-19 and 2006-08-20 in the minimal deep cluster, 2006-09-03 and 2006-09-04 in the southwestern cluster, and 2022-09-06 and 2022-09-07 in the widespread cluster), meaning that its organization of deep convection remained in a similar pattern 24 hours after.

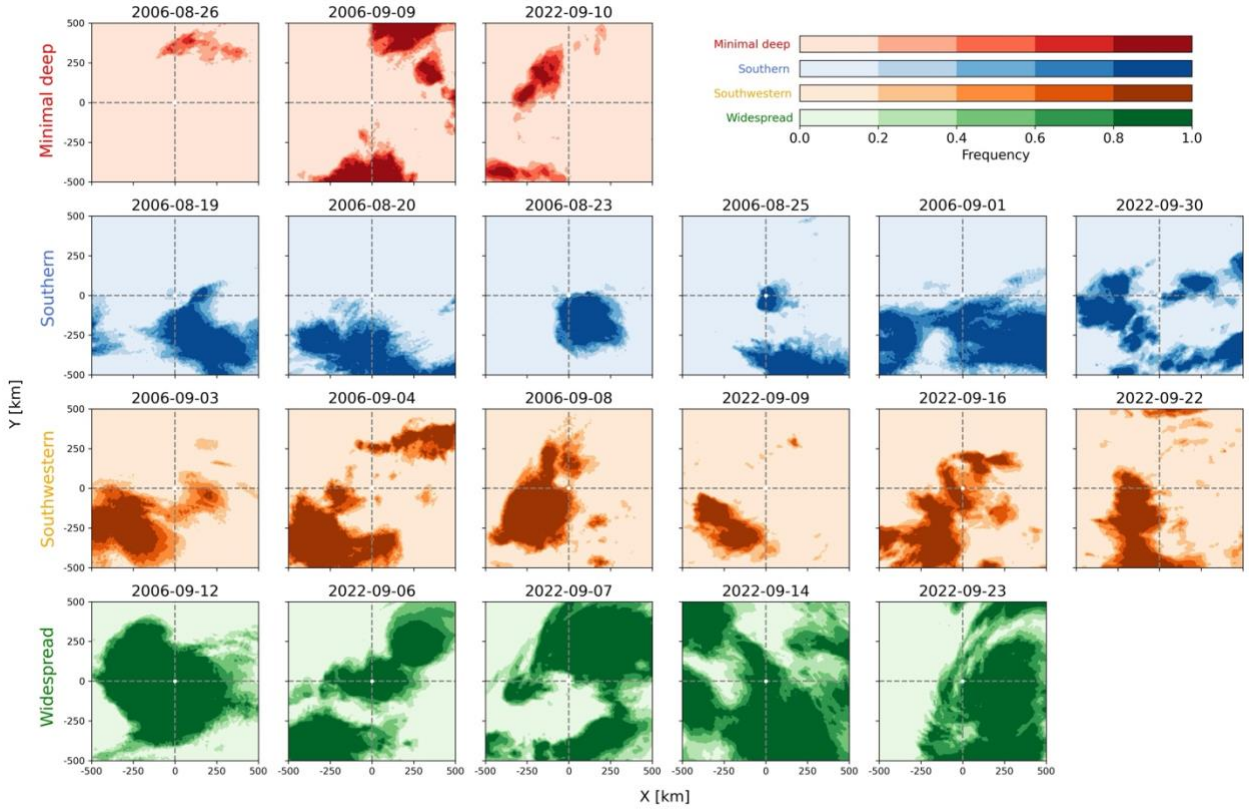

Figure 5. Frequency of deep convection over 6 hours for all cases, grouped by cluster of spatial distribution of deep convection.

Figure 6 shows the average structure of the frequency of deep convection for cases classified under each cluster. From these composites we can depict a clear representation of the patterns of deep convection previously identified in Fig. 5. Removal of the first and second day of dependent pairs that were classified under the same cluster was tested, but the overall patterns of where the convection is enhanced were generally unchanged (not shown). From this composite analysis, differences in how frequent the deep convection is across the clusters can be seen. Magnitudes of frequency of deep convection in the composites of minimal deep and south focused clusters reach a lower threshold, up to 60-80%, compared to the southwestern and widespread clusters, which show large areas of 80-100% frequency of deep convection.

The first cluster shows minimal isolated deep convection with two enhanced areas away from the PV centroid, one in the northeast quadrant and other in the southwest. However, shallow/moderate convection is depicted all around the PV centroid and occurring most frequently (60-100%) in the upper two quadrants, although its spatial distribution is not as coherent. The second composite shows deep convection present in most southern two quadrants, although a higher frequency can be depicted in the southeast quadrant (40-80%) compared to the southwest quadrant (20-40%). The third cluster shows a symmetric enhancement of deep convection in the southwest quadrant with the frequency decreasing away from the area. The fourth cluster shows deep convection spanning across all quadrants, even showing a banded structure, with deep convection being most frequent north of the PV centroid (80-100%). The south and widespread cluster show shallow/moderate convection mostly surrounding where the deep convection is found. A similar structure is depicted in the southwestern cluster, where shallow is present where deep is not. This cluster shows a particular enhancement of shallow/moderate convection in the southeast quadrant, with this type of convection being most frequent on average than the south and widespread cluster. It is important to note that convection (either shallow/moderate or deep) is present almost in the entirety of the 1000 x 1000 km domain for all cases, which indicates that the meso-scale analysis is capturing the spatial extent of convection in the waves.

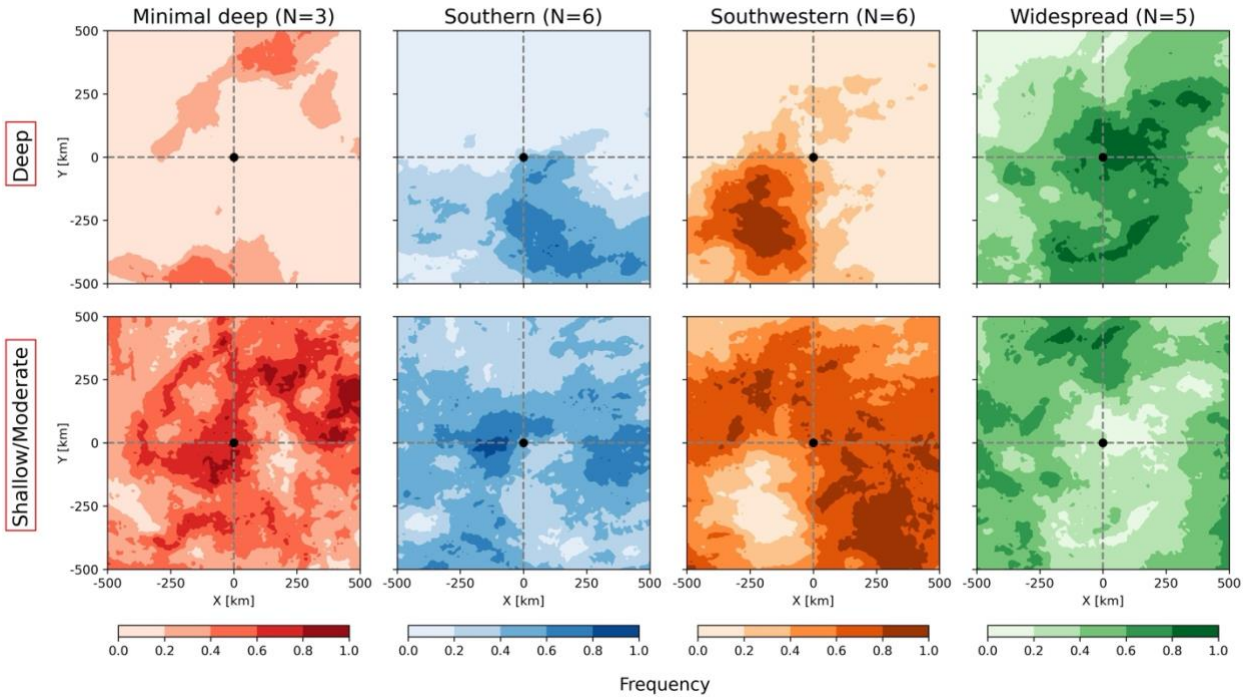

Figure 6. Average frequency of deep convection (top) and shallow/moderate convection (bottom) for cases within a cluster of deep convection.

3.2 Dynamics and its relationship to deep convection

Previous literature on AEW has identified two track paths based on a wave's interaction with the AEJ. The southern track waves have been found to be more convectively active than northern track waves due to interactions with the ITCZ. We assessed whether N-S position, E-W position, and wave motion differences would influence how the deep convection was spatially distributed around the centroid. Figure 7 shows the locations and wave motions of each case at 1200 UTC, and the respective deep convection cluster. PV centroids are widely distributed in the study region, between 14°W- 35°W, and 8°N -19°N, and wave speeds ranging between 4.7 m/s and 15.6 m/s. An easterly motion dominates across cases, although there are some latitudinal differences. Waves above 14°N show more of a northerly component in the motion, while waves located latitudinally lower tend to have a southerly component in the motion. We hypothesized

that waves characterized by south focused convection would be located in a lower latitude, as the ITCZ could be influencing this enhanced deep convection to the south, but from Fig. 7 we see a very scattered distribution, which appears to be seemingly stochastic. There is no evidence of any preference for different deep convective pattern clusters with certain areas of the domain, neither S-W nor E-W. Our analysis suggests that the location of deep convection doesn't have much of a relationship with the latitude or longitude at which the waves were sampled at or the speed at which they are moving with the spatial distribution of deep convection, suggesting there are other dominant factors at work.

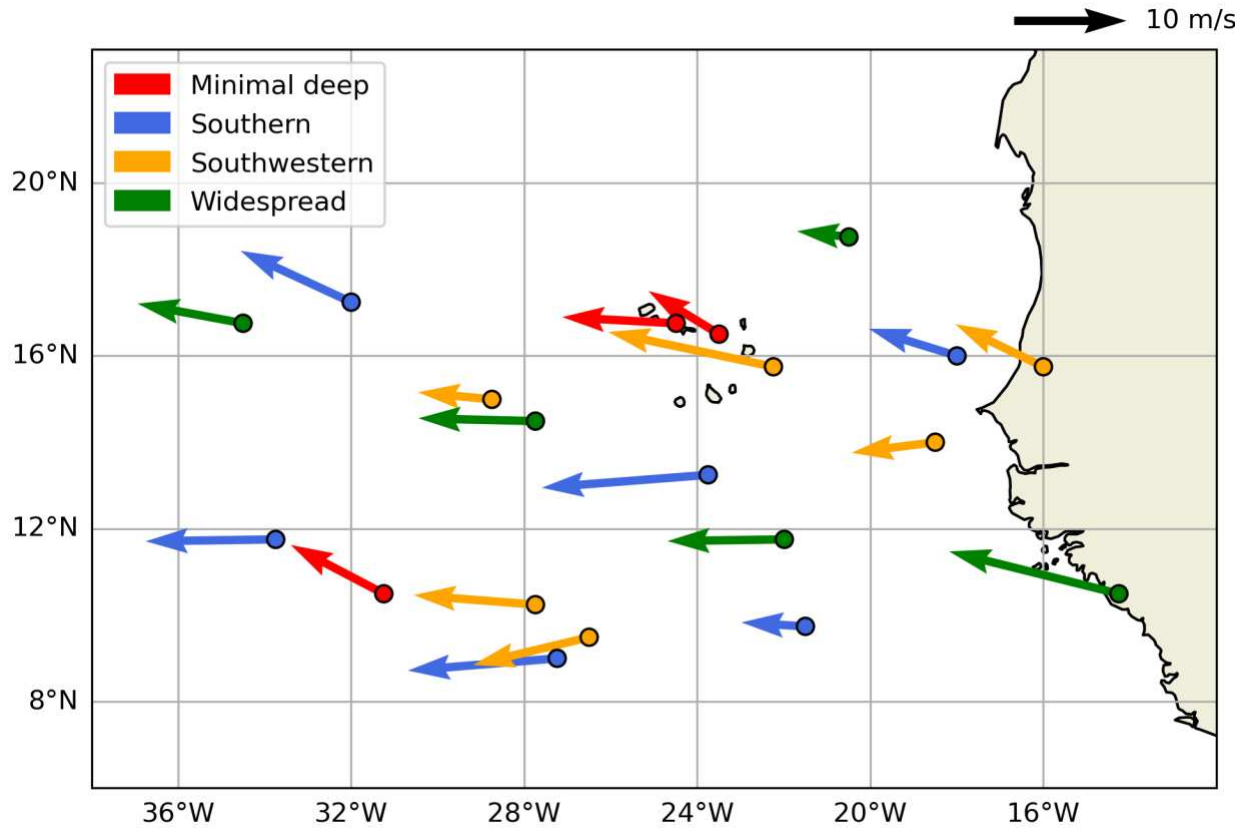

Figure 7. Positions of PV centroids at 1200 UTC for each case, wave motion vector and classification of deep convection cluster.

Next we explored how the larger scale divergence profiles relate to the convective structure, distinguishing between convective and stratiform modes. In tropical precipitation, a convective profile is generally characterized by convergence at low-levels and divergence aloft, and a stratiform profile by divergence at low levels, convergence at mid-levels, and divergence aloft (Houze 1997). We calculated the integrated divergence profile for each quadrant including a center quadrant (5 quadrants in total) over a 500 x 500 km area at each vertical level and performed the average for cases in each cluster (Fig. 8). The composite integrated divergence profile in the quadrant where deep convection is most common (thick lines) show the largest magnitudes of low-level convergence in the south, southwestern and widespread clusters, compared to the other quadrants. The analysis suggests that the low level convergence is consistent with where the deep convection is occurring with a frequency of more than 60%.

The south cluster on the quadrant where deep convection is most enhanced (lower right quadrant) shows a classic convective profile with convergence at low levels and divergence aloft, and the lower left quadrant where deep convection is up to 60% frequent, shows a mix between a more convective like profile at low to mid-levels, and more stratiform-like in the mid to upper levels. A very similar profile to the latter can be seen in the profiles for quadrants showing the most frequent deep convection in the southwestern and widespread cluster. The profiles in the latter are characterized by convergence up to 3 km, small divergence close to 4 km, convergence between 5- 9 km, and lastly divergence aloft. The profile pattern is similar to those seen on the mean profiles of divergence measured by an airborne Doppler radar during the TOGA COARE campaign and other prior studies (Houze 1997). The signal for the northeast quadrant, where deep convection is most frequent in the minimal deep cluster, shows a very small convergence near the surface, high variability in the mid levels, and weak divergence at upper levels. The

magnitudes of the convergence at the surface and divergence aloft are small compared to the other clusters. We hypothesize that since the area of frequent deep convection is less than 50% of the quadrant, the area integrated divergence is averaging out some of the mass divergence that may be happening at smaller spatial scales in this cluster.

Areas in the south cluster where shallow/moderate convection is most frequent (all quadrants except lower right) show convergence at low levels and diverging mid-levels in the upper left and center quadrant, which would be consistent with shallower convection. The upper right quadrant in this cluster where shallow /moderate convection is 20-80% frequent, shows an interesting divergence at 2 km, that deviates from the structure seen in the former two quadrants. Overall, the cluster showing deep convection enhancement to the south is characterized by convective clouds of varying heights depending on the quadrant and showing forcing for ascent all around. The southwestern cluster for the upper right, upper left and lower right quadrant where the frequency of shallow/moderate convection is between 20- 100% shows a stratiform signal aloft, with convergence at mi-levels and divergence higher up. Lastly the widespread cluster, in the upper left, upper right and lower right quadrant show convergence up to 9 km and divergence aloft, suggesting a more mature convective structure. Interestingly the lower left quadrant shows strong convergence at low levels, diverging between 2-6 km, converging 6-9 km and diverging after. For all the clusters, the large scale forcing for ascent is consistent with where the convection was observed, particularly in areas where deep convection was frequent. The satellite and SAMURAI analyses are not completely independent since the ERA5 background estimate assimilates the satellite information, but the good consistency between the dynamic fields and observed convection provides confidence in the analysis.

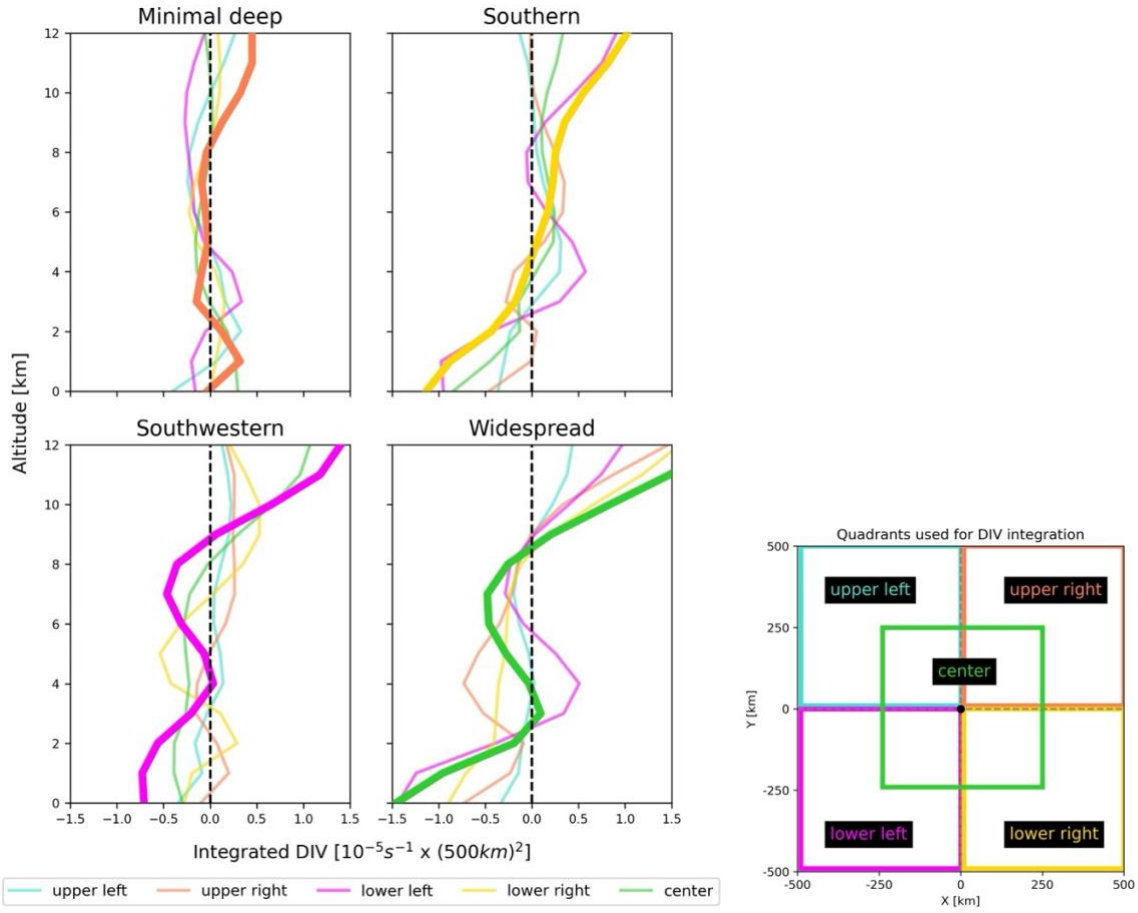

Figure 8. Integrated mean SAMURAI divergence over a 500 x 500 km quadrant with altitude. Thick line represents the quadrant where deep convection is enhanced in each cluster group.

Figure 9 shows the SAMURAI analysis of PV (where 10^{-6} $Km^2kg^{-1}s^{-1}$ = 1PVU), RH, and wave relative wind, for all cases at 6 km, organized by deep convection cluster. This level was selected as it is where the PV is maximized based on a cross-section analysis (shown later in Fig. 11). We find that areas of high PV (> 1.2 PVU), are generally in the vicinity of high RH areas (> 85%) for all cases, but there is some variability where they are maximized relative to the PV centroid. PV is maximized for most cases in the vicinity of the PV centroid, but the pointwise maxima are not collocated with the centroid maxima. The displacement may be due to changes in the PV maxima in the vertical, since the PV centroids are maximizing area and depth

integrated PV in the lower troposphere. Comparing the PV and RH structures to the frequency of deep convection in a case to case basis reveals substantial spatial overlap with deep convection areas, especially for cases in the cluster characterized by widespread convection. Cases in the southwestern cluster show great overlap of high PV and high RH areas but these seem to be displaced east of where the deep convection is most frequent (in lower left quadrant), with the exception of case 20060903 which shows PV and RH enhancement right where the deep convection is found. This hypothesis is supported by the RH in cases from the south focused cluster that also show overlap with where the deep convection is, but a greater variability in the location of PV is noted. For example, cases 20060819, 2006825 and 20220930 show an enhancement of PV away from where the deep convection is most frequent, but 20060823 and 20060901, which have a greater magnitude of PV (reaching 2 PVU) are collocated with the highest RH and deep convection location. In general, the regions of PV that exceed 1.6 PVU are collocated with the highest RH and where deep convection is most frequent. Cases associated with the strongest values of PV show a wave relative wind that rotates counterclockwise around the PV centroid. The rotation is to be expected given the definition of PV, but for cases with weaker PV and lower values of RH (e.g 20060819, 20060820, and 20220910) this rotation seems to be weaker or not present at all.

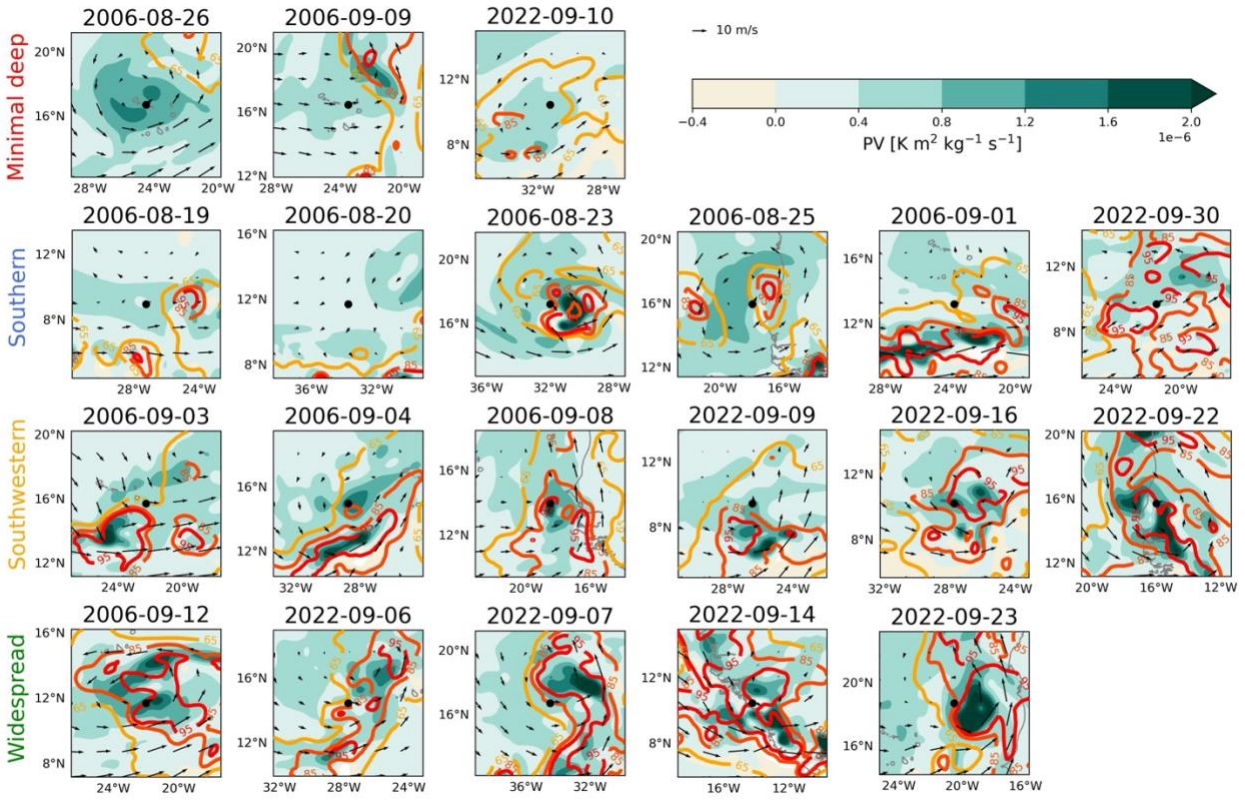

Figure 9. SAMURAI Analysis of potential vorticity (PV) (filled contours), relative humidity (RH %) (contours), and wave relative wind (black vectors) at 6 km, centered on PV centroid for all cases (N= 20).

Despite the variable structures in the SAMURAI fields in a case to case basis, some commonalities can be seen across the cases within a deep convection cluster classification. To examine these commonalities we performed a composite analysis of thermodynamic and dynamical conditions by averaging the SAMURAI fields for cases within each deep convection cluster. The composite analysis allows us to better analyze the differences in the dynamical fields in relation to the strength and location of deep convection. The composite analysis (Fig. 10) confirms that high PV spatially overlapping with high RH areas at 6 km is a robust feature across the clusters. In the composites, the southwestern and widespread clusters are associated with the strongest values of PV on average, and broad areas of high humidity, exceeding 90%, are collocated with each other. The overlap is most prominent in the widespread cluster where we

find that PV and RH are enhanced east of the PV centroid and in the upper right quadrant, overlapping with where the sustained deep convection is found in this composite (Fig. 10). The southwestern cluster shows PV and RH maximizing at 6 km near and south of the PV centroid, to the west of where the sustained deep convection is found. This westward displacement of the deep convection relative to the enhanced PV and RH areas could be that the deep convection identified in this quadrant is a stratiform cloud that is covering convective clouds associated with what we are seeing in the dynamical fields and are not being captured by the satellite analysis. From the integrated divergence calculations (Figure 8) we see a stratiform signal aloft in this quadrant, which would support this hypothesis.

The south cluster shows a PV maxima east of the PV centroid and an elongated area of PV in the lower two quadrants. Highest RH (<80%) is found in the lower right quadrant, same area where the sustained convection maximizes. The signal in the minimal deep cluster is not as clear, with PV enhancement in the center quadrant, and a broad area of maximum RH (<80%) in the upper right quadrant, where an area of deep convection is found. It is important to note that the frequency of convection analysis and the SAMURAI analysis are independent of each other, but clustering the SAMURAI analyses by the spatial patterns of deep convection reveals coherent patterns in the thermodynamics and dynamics that are consistent with the patterns found with convection. The consistency in location and intensity, given the independency of the two analyses suggests a strong correlation between PV and high RH with frequency of deep convection.

The counterclockwise rotation of wave relative wind vectors around the PV centroid observed across all clusters reveal that the PV centroid methodology applied here captures the center of wave relative circulation at the meso-alpha scale. A stronger wave relative flow is

observed for all clusters in the lower two quadrants (south of the PV centroid) compared to the upper quadrants. The average wave relative wind speed in the lower two quadrants is 7.3 times greater than in the upper two quadrants in the minimal deep cluster, 3.4 times in the southern cluster, 5.7 times in the southwestern cluster and 8.7 times in cluster 4. The magnitude of wave relative wind at 6 km, particularly in the lower two quadrants shows increases with magnitude of PV and RH, with the southwestern and widespread cluster showing the greatest. The average low to mid-level vertical wind shear (VWS) for each cluster was calculated and shown in Fig. 10. The south cluster and southwestern cluster show similar magnitudes of wind shear around 4 m/s, while the widespread and minimal deep cluster are lower at 2.81 m/s and 2.99 m/s respectively. The wind shear vector direction was found to be similar across clusters spanning between east south-east and south south-east. Given the minor differences in the wind shear across clusters, we decided to not pursue it further.

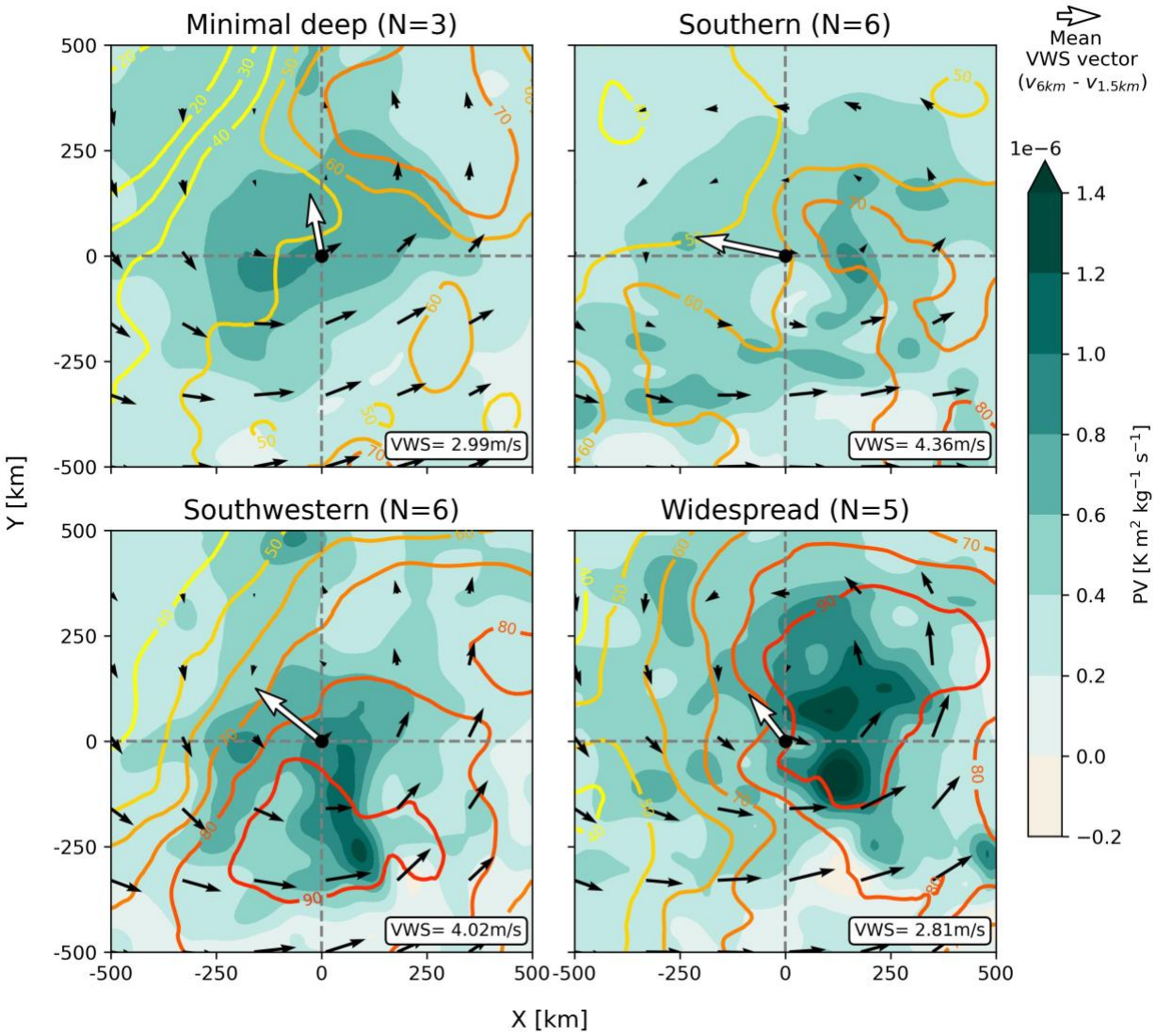

Figure 10. Average SAMURAI Analysis of potential vorticity (PV) (filled contours), relative humidity (RH %) (contours), and wave relative wind (black vectors) at 6 km for cases within each deep convection cluster. Average vertical wind shear (6 km- 1.5 km) magnitude and vector are shown in white.

Recent work (Russell 2020, Boehm and Bell 2021) offer conceptual models for understanding PV displacement in the vertical in AEWs. The model suggested by Russell 2020 highlights the presence of a low level PV tendency ahead of the trough due to condensational heating from convection, and a displaced PV tendency aloft due to diabatic heating from trailing stratiform convection, supporting the idea of convection driven tilted PV tower. We explore the

variability in PV towers based on deep convection cluster. Cross sections of PV (Fig. 11) show extensive areas of PV maxima across the domain, but large differences on the vertical extent and magnitude of these PV areas based on where the deep convection is most frequent. Both the southwestern and widespread cluster show an elongated PV maxima extending vertically located east of the PV centroid. The structure of PV in these two clusters also shows a westward elongation of this PV anomaly at 6-8 km. This elongation is also seen for the cross-sections along the center and south in the southern cluster and the north and center cross-sections in the widespread cluster. PV towers in the minimal deep cluster maximize west of the PV centroid in the cross-section along the south and east of the PV centroid in the north cross-section. Maximum PV towers for these three clusters collocate with where the deep convection is most frequent in each cross-section. The southwestern cluster exhibits a different pattern in the PV structure with PV maximas centered in the domain of the north and center cross-sections, and two PV towers in the south cross-section. The PV tower associated with the greatest magnitude of PV (at least up to 1.2 PVU) is located east of where the deep convection is found. Comparing the magnitude of PV with the frequency of deep convection in the cross-sections in each cluster reveals that cross-sections that have a higher frequency of deep convection show PV towers with greater magnitudes in general for all clusters except for the south cluster. In the south cluster, PV is greatest across the center cross-section, while deep convection is most frequent along the south cross-section. The greatest enhancement of PV is found at mid-levels between 6-8 km for all the clusters, although there are notable differences based on where the deep convection is found. The southwestern and widespread clusters are associated with the greatest magnitudes of PV, exceeding 1.2 PVU between 6-8 km in cross-sections with the greatest frequency of deep

convection, and are associated with the tallest PV towers. These two clusters also showed to have the greatest magnitudes of PV in the 2D analysis at 6 km and statistical analysis.

All cross-sections show moist low levels collocated with where deep convection is most frequent, but large differences are noted across clusters on how this high moisture extends vertically. Moisture in the minimal deep cluster highlight moist low levels where deep convection is present (south and center), although high moisture (>80%) doesn't extend as high as in the southwestern and widespread clusters. These differences highlight that in cases with higher frequency of deep convection one might expect more moisture extending up to mid-levels. In the south cluster, RH of 70% or higher extends up to 6 km in the center and south cross-sections in areas where deep convection is most frequent, while RH >70% in the north cross-section doesn't go above 2 km, where the frequency of deep convection is of 0-20% based on the IR composites (Fig. 6). In the southwestern cluster we find plenty of moisture of at least 80% all widespread through the domain extending up to 8 km in the south cross-section where deep convection is most frequent. Moisture is less abundant in cross sections where deep convection is not as frequent, RH up to 70% at 7 km along the center and north, where deep convection is 20-60% frequent. The widespread cluster shows very moist (>80%) low to mid levels extending up to 8 km along the north and center where deep convection is most frequent, and decreasing in vertical extent in the south cross-section. Overall, we find that higher values of RH (>90%) and high moisture extend further vertically in cross-sections that encounter a greater frequency of deep convection (Southern: south cross-section, Southwestern: south cross-section, Widespread: center cross-section) with high moisture (>70%) going up to 10 km in the vertical in the widespread cluster.

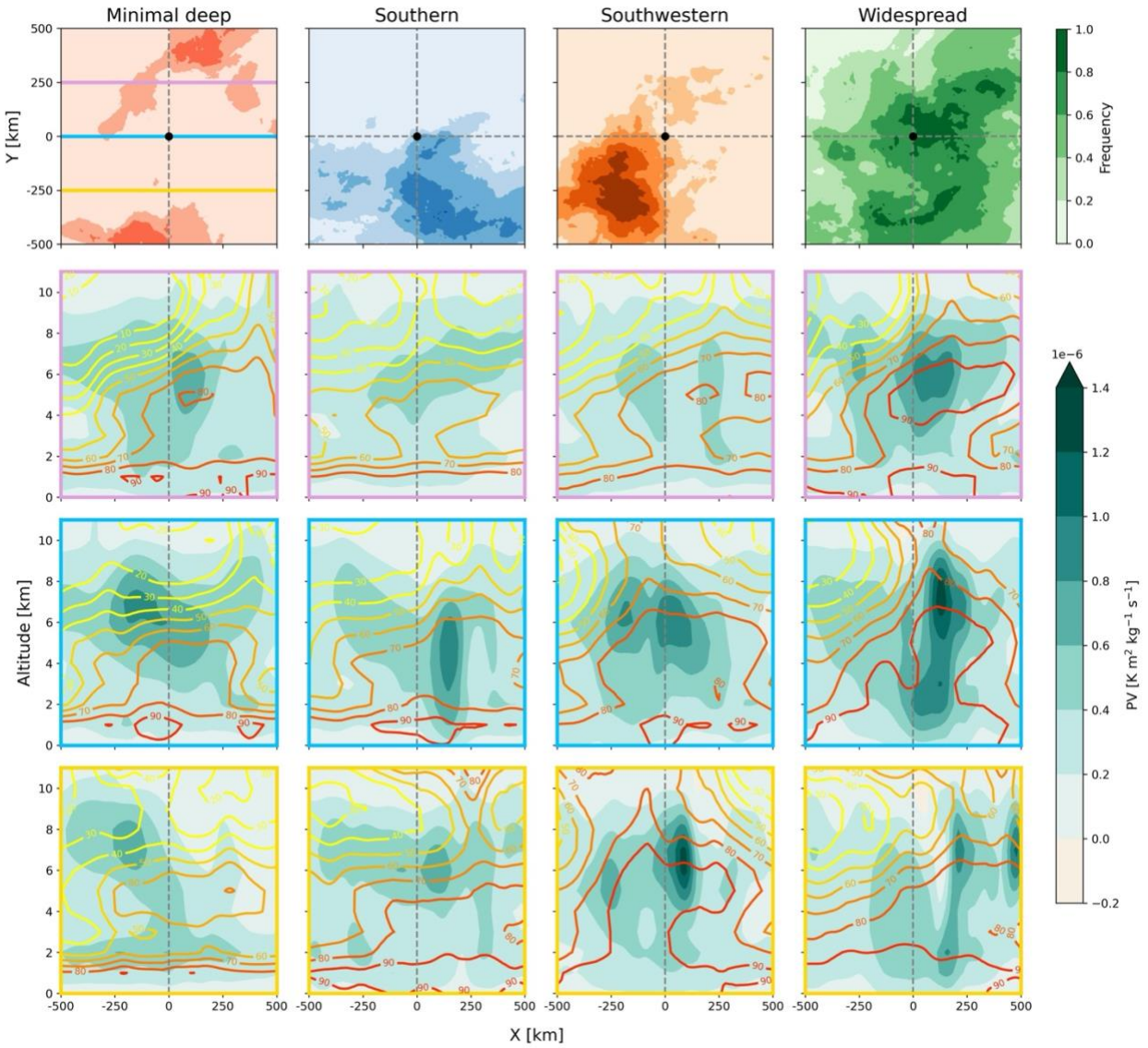

Figure 11. Average frequency of deep convection (first row), and east to west vertical cross-sections (along y= -250 km (south), y= 0 km (center), and y= 250 km (north)) of the average PV (filled contours) and RH (contours) SAMURAI analysis for each cluster.

From Fig. 12 we can assess the probability distribution functions (PDFs) of PV and RH for grid points in cases within each cluster where deep convection is frequent 80-100% of the time, and grid points with no deep convection (hereafter clear/shallow/moderate convection). It is important to clarify that these PDFs were calculated from the frequency of deep convection of individual cases grouped by cluster, not the composite frequency of deep convection. From the

frequency of deep convection on individual cases (Fig. 5) we see that the signal for where the deep convection is found is captured by the 80-100% level. Across all clusters it is evident that PV and RH are greater when there is deep convection present compared to the clear/shallow/moderate convection distributions. The statistical significance to the 95% level of the mean distribution of PV and RH between deep convection and clear/shallow/moderate convection was tested through a Welch's t-test. Results showed p-values all less than 0.05, suggesting statistically significant differences between both distributions for all clusters. It is important to note that given this analysis was made in a gridpoint basis, this could incur in some spatial autocorrelation. The large sample size and the fact that some cases are the same wave, could have influenced these very low p-values, as well.

The southwest and widespread cluster showed the greatest increase in the PV distribution between no deep convection to 80-100% deep convection with a difference in the distribution median of 1.5 PVU and 1 PVU, respectively. These clusters are associated with the greatest magnitudes of PV, which we saw from Fig. 10, with the third quartile between 0.4 PVU and 0.6 PVU for both distributions. For the south and minimal deep clusters, the increase in the distribution median is less than 0.5 PVU. Interestingly, the three major deep convection clusters, south, southwestern and widespread, show a distribution median close to 90% RH. The minimal deep cluster distribution shows a median value of 70% in RH. This difference confirms results from previous analysis suggesting that cases in the south, southwestern, and widespread clusters are associated with high moisture at 4 km and that this high moisture is correlated with the presence of deep convection.

Regarding differences in RH between 80-100% deep convection and clear/shallow/moderate convection across the clusters, cases with southern enhancement of deep

convection showed the greatest increase in the distribution median of about 30%. Meanwhile the southwestern cluster showed an increase of 15% and the widespread cluster of 20%. The minimal deep cluster showed an increase of about 8% in the distribution mean with presence of deep convection. The minimal deep convection having lower increases in the distribution mean for PV and RH compared to the other clusters strengthens the conclusion that both PV and RH are correlated with deep convection areas.

Variability in the distribution of PV where deep convection is present is much higher than the clear/shallow/moderate groups. The reverse is seen in RH, where the clear/shallow/moderate groups are highly variable, spanning from low humidity to 100%, compared to the 80-100% deep convection distributions that span between 70-100% for the south, southwestern, and widespread cluster. These differences in the variability of PV and RH distributions between the deep convection and the clear/shallow/moderate convection suggest that high moisture on itself is not sufficient for deep convection, but it is better correlated than PV with where the deep convection is found.

We see the PV distribution in the south and widespread clusters spanning values below (even negative PV values), and above the distribution maximum and minimum for the clear/shallow/moderate convection groups. In the southwestern cluster we see an entire increase in the distribution, suggesting this cluster has the greatest correlation between PV and frequency deep convection from all the clusters. This cluster showed the eastward displacement in the maximum PV from the deep convection. However, the small variability in frequency of deep convection in the cases among this cluster depicted from the symmetric enhancement in Fig. 6 could be influencing this result. Values of RH for 80-100% frequency of deep convection in the south, southwestern, and widespread cluster span between 70- 100% in the 25^{th}-75^{th} quantile,

showing an overall moist environment across the domain for these 3 clusters, while the minimal deep cluster shows less moisture on average. Variability in the values of RH is high for pixels where there is no deep convection present values ranging between 20-100% in the south cluster and 30-100% in the southwestern and widespread clusters.

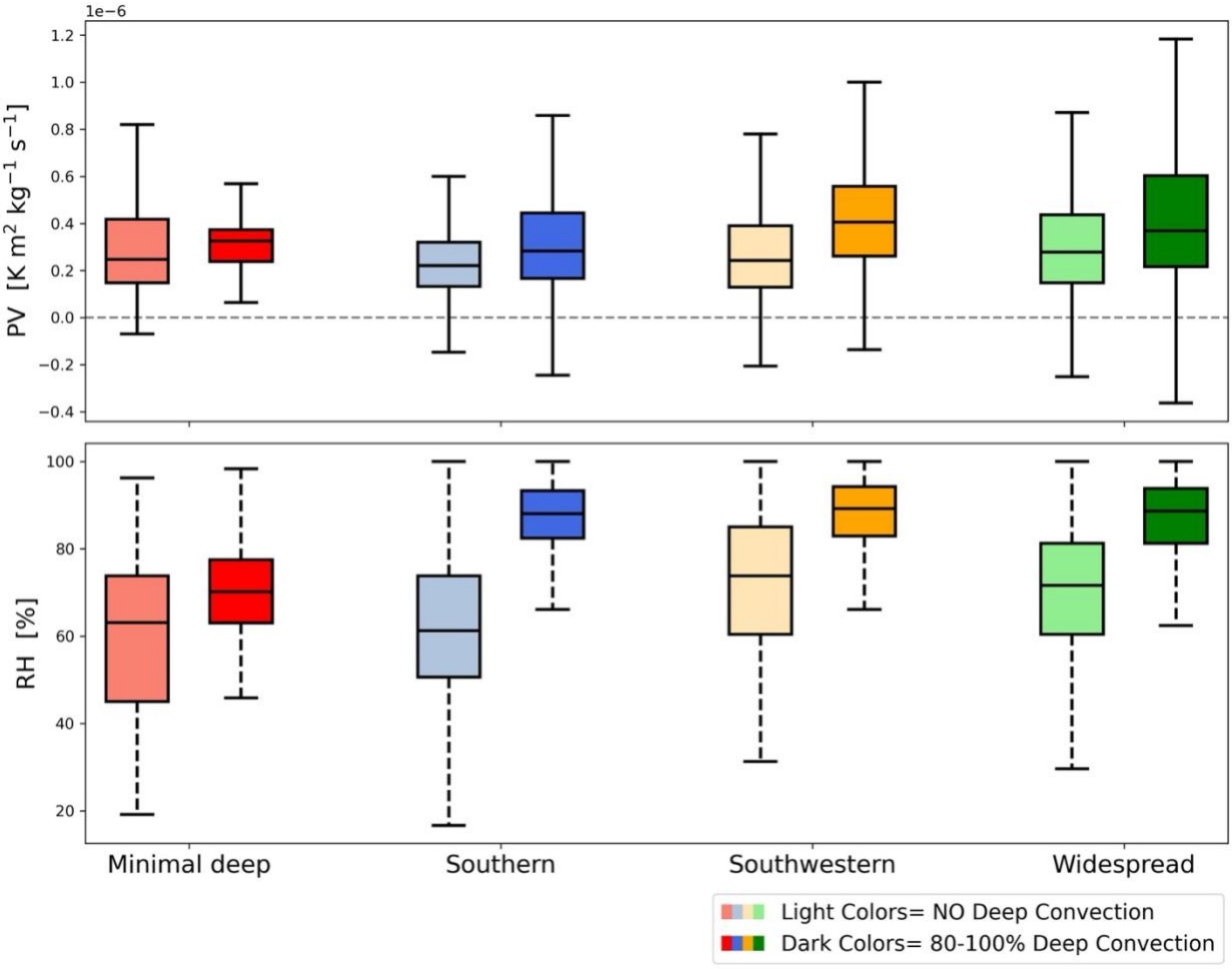

Figure 12. Comparison of statistical distribution of PV (solid whiskers) and RH (dashed whiskers) pixels where 80-100% frequency of deep convection are found (dark colors) and where there is only clear/shallow/moderate convection (light colors) for cases within each cluster of deep convection at 4 km. The box represents the interquartile range, with the median value in the center, and the lower and upper bound of the whisker are the minimum and maximum value respectively, without outliers.

CHAPTER 4- Conclusions

In this study we analyze how the spatial structure of the frequency of deep convection in 20 African Easterly Waves (AEWs) relate to the potential vorticity (PV), and relative humidity (RH), structure from a composite analysis. We employ a novel methodology to construct vortex centric SAMURAI (Spline Analysis at Mesoscale Utilizing Radar and Aircraft Instrumentation) analyses at the meso-alpha scale, incorporating ERA5 reanalysis and dropsonde, flight level, DAWN, and HAMSR observations from the NASA DC8 collected during the NAMMA and CPEX-CV field campaigns. The SAMURAI fields capture the wave relative circulation around the PV centroid across cases with the magnitude of the wave relative wind being proportional to the magnitude of PV, supporting the value of using a PV centroid approach. We aim to answer two main research questions: 1) What are the convective characteristics of AEWs using a vortex-centric approach?, and 2) How do moisture and potential vorticity relate to the convective organization in African easterly waves at the meso-alpha scale?

Regarding the first question, we analyze the frequency of shallow/moderate and deep convection satellite brightness temperature centered on a PV centroid for each respective case. Four clusters of how the frequency of deep convection is spatially distributed from satellite images were identified. These were characterized by deep convection enhancement south of the PV centroid, in the southwest quadrant, widespread, and minimal deep. We find that deep convection located southwest of the PV centroid and distributed widespread around the vortex are the most common, with frequency exceeding 80% in enhanced areas, although shallow/moderate convection is found in high frequency surrounding the areas of enhanced deep convection for all clusters.

Regarding the second question, we find that RH and PV are correlated with the intensity and spatial distribution of deep convection frequency. From the composite analysis of SAMURAI fields areas of high PV are generally in the vicinity of high RH areas at 6 km (Fig. 10), which was also depicted from the individual case analysis (Fig. 9), and this collocation is enhanced in areas with a higher frequency of deep convection. These areas of enhanced frequency of deep convection are also consistent with low-level convergence (Fig. 8). The intensity and vertical extent of PV towers and high moisture in low to mid levels in the cross-sectional analysis were shown to be correlated with the magnitude and location of frequency of deep convection as well. Nonetheless, a large variability in values of PV in pixels with presence of deep convection >80% frequent is noted, particularly for cases in the widespread deep convection cluster. Overall RH showed a greater signal of where the deep convection can be found, but a larger variability than PV when compared from the PDF analysis showed in Fig. 12.

Figure 13 shows a schematic portraying the spatial and magnitude relationships between PV, RH and deep convection depicted in our composite analysis. The minimal deep cluster shows displaced deep convection away from where the PV centroid and enhancement of mid-level PV is found. However, the mid-level PV maximum does overlap with the presence of shallow/moderate convection shown in Fig. 6 for this cluster. Moisture is enhanced where the northern deep convection area is found, correlating better than PV in this case. There isn't a clear overlapping of the three factors in this cluster, which could be influenced by the small sample size of N= 3. The cluster where enhanced deep convection is found in the southern two quadrants shows an elongated enhancement of PV at mid-levels, and moderate RH more pronounced in the southeast quadrant, collocating with the area where the greatest frequency of deep convection is found. The southwestern focused deep convection cluster is characterized by a higher PV

collocated with high moisture at mid-levels, that are both displaced east of where the deep convection is most frequent. Lastly the widespread deep convection cluster shows an enhanced PV with high RH area east of the PV centroid that is collocated with the presence of deep convection. Both the minimal deep and the south clusters are associated with a lower frequency of deep convection in general, and lower relative magnitude of PV and RH when compared to the southwestern and widespread cluster. In a sense, the clusters show a progression of intensity of deep convection, from minimal deep to widespread, and consequently an increase in magnitudes of RH and PV and spatial overlap of these factors.

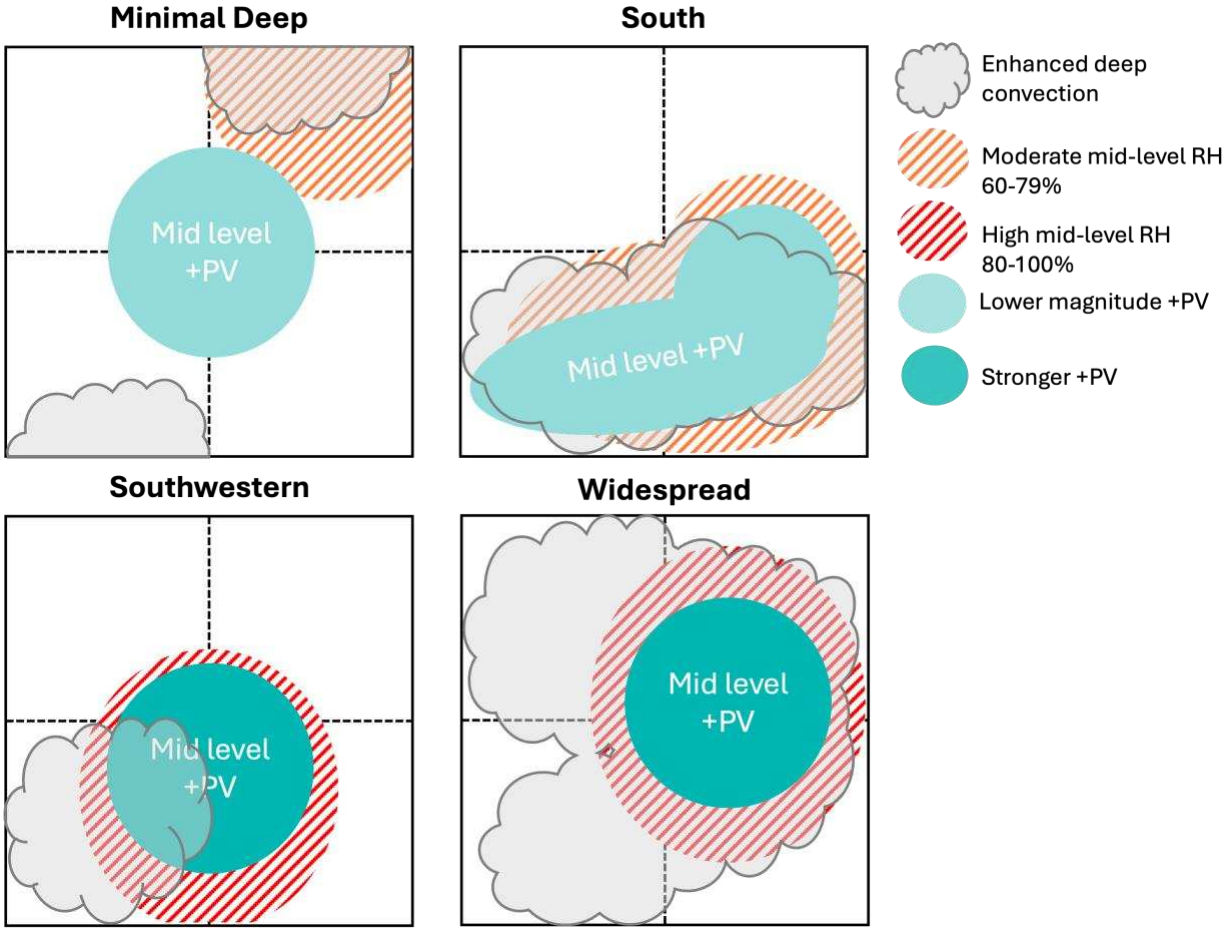

Figure 13. Schematic comparison of the four clusters and their areas of enhanced frequency of deep convection, and differences in the magnitude of the RH and PV at mid-levels.

Our results inform research regarding convective structure in AEWs and potential dynamical and thermodynamical factors that lead to those structures. Given that our analysis is just at 1200 UTC, further research should focus on analyzing the temporal evolution of the highlighted PV and RH enhancement and its relation to the location and intensity of deep convection. A temporal analysis using ERA-5 and modeling could help assess cause and effect of these relationships and properly compare with conceptual frameworks that have been suggested by literature. Additionally, we hope to test whether the clusters of deep convection organization found in this study and other findings hold for a larger sample size. The use of ERA-5 by itself to increase the sample size and test the dynamical relationships in a temporal scale may be appropriate but would involve coarser spatial scales due to the lack of field campaign observations.

REFERENCES

Adames, Á. F., & Ming, Y. (2018). Interactions between Water Vapor and Potential Vorticity in Synoptic-Scale Monsoonal Disturbances: Moisture Vortex Instability. https://doi.org/10.1175/JAS-D-17-0310.1

Agudelo, P. A., Hoyos, C. D., Curry, J. A., & Webster, P. J. (2011). Probabilistic discrimination between large-scale environments of intensifying and decaying African Easterly Waves. Climate Dynamics, 36(7), 1379–1401. https://doi.org/10.1007/s00382-010-0851-x

Avila, L. A., & Pasch, R. J. (1992). Atlantic Tropical Systems of 1991. https://journals.ametsoc.org/view/journals/mwre/120/11/1520-0493_1992_120_2688_atso_2_0_co_2.xml

Bedka, K. M., Nehrir, A. R., Kavaya, M., Barton-Grimley, R., Beaubien, M., Carroll, B., Collins, J., Cooney, J., Emmitt, G. D., Greco, S., Kooi, S., Lee, T., Liu, Z., Rodier, S., & Skofronick-Jackson, G. (2021). Airborne lidar observations of wind, water vapor, and aerosol profiles during the NASA Aeolus calibration and validation (Cal/Val) test flight campaign. Atmospheric Measurement Techniques, 14(6), 4305–4334. https://doi.org/10.5194/amt-14-4305-2021

Bell, M. M., & Montgomery, M. T. (2019). Mesoscale Processes during the Genesis of Hurricane Karl (2010). https://doi.org/10.1175/JAS-D-18-0161.1

Bell, M. M., Montgomery, M. T., & Emanuel, K. A. (2012). Air–Sea Enthalpy and Momentum Exchange at Major Hurricane Wind Speeds Observed during CBLAST. https://doi.org/10.1175/JAS-D-11-0276.1

Bercos-Hickey, E., & Patricola, C. M. (2024). African Easterly Wave Strength and Observed Atlantic Tropical Cyclone Genesis and Characteristics. Journal of Geophysical Research: Atmospheres, 129(10), e2024JD040858. https://doi.org/10.1029/2024JD040858

Berry, G. J., & Thorncroft, C. (2005). Case Study of an Intense African Easterly Wave. https://doi.org/10.1175/MWR2884.1

Boehm, A. M., & Bell, M. M. (2021). Retrieved Thermodynamic Structure of Hurricane Rita (2005) from Airborne Multi–Doppler Radar Data. https://doi.org/10.1175/JAS-D-20-0195.1

Brammer, A., & Thorncroft, C. D. (2015). Variability and Evolution of African Easterly Wave Structures and Their Relationship with Tropical Cyclogenesis over the Eastern Atlantic. https://doi.org/10.1175/MWR-D-15-0106.1

Brammer, A., Thorncroft, C. D., & Dunion, J. P. (2018). Observations and Predictability of a Nondeveloping Tropical Disturbance over the Eastern Atlantic. https://doi.org/10.1175/MWR-D-18-0065.1

Brown, S. T., Lambrigtsen, B., Denning, R. F., Gaier, T., Kangaslahti, P., Lim, B. H., Tanabe, J. M., & Tanner, A. B. (2011). The High-Altitude MMIC Sounding Radiometer for the Global Hawk Unmanned Aerial Vehicle: Instrument Description and Performance. IEEE Transactions on Geoscience and Remote Sensing, 49(9), 3291–3301. https://doi.org/10.1109/TGRS.2011.2125973

Burpee, R. W. (1972). The Origin and Structure of Easterly Waves in the Lower Troposphere of North Africa. https://journals.ametsoc.org/view/journals/atsc/29/1/1520-0469_1972_029_0077_toasoe_2_0_co_2.xml

Cha, T.-Y., & Bell, M. M. (2023). Three-Dimensional Variational Multi-Doppler Wind Retrieval over Complex Terrain. https://doi.org/10.1175/JTECH-D-23-0019.1

Chen, T.-C., Wang, S.-Y., & Clark, A. J. (2008). North Atlantic Hurricanes Contributed by African Easterly Waves North and South of the African Easterly Jet. https://doi.org/10.1175/2008JCLI2523.1

Dominguez, C., Done, J. M., & Bruyère, C. L. (2020). Easterly wave contributions to seasonal rainfall over the tropical Americas in observations and a regional climate model. Climate Dynamics, 54(1), 191–209. https://doi.org/10.1007/s00382-019-04996-7

Doswell, C. A., Brooks, H. E., & Maddox, R. A. (1996). Flash Flood Forecasting: An Ingredients-Based Methodology. Weather and Forecasting, 11(4), 560–581. https://doi.org/10.1175/1520-0434(1996)011<0560:FFFAIB>2.0.CO;2

Enyew, B. D., & Mekonnen, A. (2022). The Interaction between African Easterly Waves and Different Types of Deep Convection and Its Influence on Atlantic Tropical Cyclones. Atmosphere, 13(1), Article 1. https://doi.org/10.3390/atmos13010005

Giangrande, S. E., Feng, Z., Jensen, M. P., Comstock, J. M., Johnson, K. L., Toto, T., Wang, M., Burleyson, C., Bharadwaj, N., Mei, F., Machado, L. A. T., Manzi, A. O., Xie, S., Tang, S., Silva Dias, M. A. F., de Souza, R. A. F., Schumacher, C., & Martin, S. T. (2017). Cloud characteristics, thermodynamic controls and radiative impacts during the Observations and Modeling of the Green Ocean Amazon (GoAmazon2014/5) experiment. Atmospheric Chemistry and Physics, 17(23), 14519–14541. https://doi.org/10.5194/acp-17-14519-2017

Greco, S., Emmitt, G. D., DuVivier, A., Hines, K., & Kavaya, M. (2020). Polar Winds: Airborne Doppler Wind Lidar Missions in the Arctic for Atmospheric Observations and Numerical Model Comparisons. Atmosphere, 11(11), Article 11. https://doi.org/10.3390/atmos11111141

Greco, S., Emmitt, G. D., Garstang, M., & Kavaya, M. (2020). Doppler Aerosol WiNd (DAWN) Lidar during CPEX 2017: Instrument Performance and Data Utility. Remote Sensing, 12(18), Article 18. https://doi.org/10.3390/rs12182951

Hall, N. M. J., Kiladis, G. N., & Thorncroft, C. D. (2006). Three-Dimensional Structure and Dynamics of African Easterly Waves. Part II: Dynamical Modes. https://doi.org/10.1175/JAS3742.1

Hersbach, H., Bell, B., Berrisford, P., Biavati, G., Horányi, A., Muñoz Sabater, J., Nicolas, J., Peubey, C., Radu, R., Rozum, I., Schepers, D., Simmons, A., Soci, C., Dee, D., Thépaut, J-N. (2023): ERA5 hourly data on pressure levels from 1940 to present. Copernicus Climate Change Service (C3S) Climate Data Store (CDS), DOI: 10.24381/cds.bd0915c6

Hopsch, S. B., Thorncroft, C. D., & Tyle, K. R. (2010). Analysis of African Easterly Wave Structures and Their Role in Influencing Tropical Cyclogenesis. https://doi.org/10.1175/2009MWR2760.1

Hoskins, B. J., McIntyre, M. E., & Robertson, A. W. (1985). On the use and significance of isentropic potential vorticity maps. Quarterly Journal of the Royal Meteorological Society, 111(470), 877–946. https://doi.org/10.1002/qj.49711147002

Houze, R. A. (1997). Stratiform Precipitation in Regions of Convection: A Meteorological Paradox? https://journals.ametsoc.org/view/journals/bams/78/10/1520-0477_1997_078_2179_spiroc_2_0_co_2.xml

Hsieh, J.-S., & Cook, K. H. (2005). Generation of African Easterly Wave Disturbances: Relationship to the African Easterly Jet. https://doi.org/10.1175/MWR2916.1

Janiga, M. A., & Thorncroft, C. D. (2016). The Influence of African Easterly Waves on Convection over Tropical Africa and the East Atlantic. https://doi.org/10.1175/MWR-D-14-00419.1

John Janowiak, Bob Joyce, Pingping Xie (2017), NCEP/CPC L3 Half Hourly 4km Global (60S - 60N) Merged IR V1, Edited by Andrey Savtchenko, Greenbelt, MD, Goddard Earth Sciences Data and Information Services Center (GES DISC), Accessed: [June 2024], 10.5067/P4HZB9N27EKU

Kavaya, M. J., Beyon, J. Y., Koch, G. J., Petros, M., Petzar, P. J., Singh, U. N., Trieu, B. C., & Yu, J. (2014). The Doppler Aerosol Wind (DAWN) Airborne, Wind-Profiling Coherent-Detection Lidar System: Overview and Preliminary Flight Results. https://doi.org/10.1175/JTECH-D-12-00274.1

Kim, M., Kim, D., Camargo, S. J., Wing, A. A., & Moon, J. (2025). The Role of Tropical Cyclone Seeds on Modulating the Seasonal Cycle of Tropical Cyclone Frequency in the North Indian Ocean. Geophysical Research Letters, 52(12), e2025GL115189. https://doi.org/10.1029/2025GL115189

Landsea, C. W. (1993). A Climatology of Intense (or Major) Atlantic Hurricanes. https://journals.ametsoc.org/view/journals/mwre/121/6/1520-0493_1993_121_1703_acoima_2_0_co_2.xml

Lawton, Q. A., Majumdar, S. J., Dotterer, K., Thorncroft, C., & Schreck, C. J. (2022). The Influence of Convectively Coupled Kelvin Waves on African Easterly Waves in a Wave-Following Framework. https://doi.org/10.1175/MWR-D-21-0321.1

Leppert, K. D., Cecil, D. J., & Petersen, W. A. (2013). Relation between Tropical Easterly Waves, Convection, and Tropical Cyclogenesis: A Lagrangian Perspective. https://doi.org/10.1175/MWR-D-12-00217.1

Lin, Y.-L., Robertson, K. E., & Hill, C. M. (2005). Origin and Propagation of a Disturbance Associated with an African Easterly Wave as a Precursor of Hurricane Alberto (2000). https://doi.org/10.1175/MWR3035.1

May, R. M., Goebbert, K. H., Thielen, J. E., Leeman, J. R., Camron, M. D., Bruick, Z., Bruning, E. C., Manser, R. P., Arms, S. C., & Marsh, P. T. (2022). MetPy: A Meteorological Python Library for Data Analysis and Visualization. https://doi.org/10.1175/BAMS-D-21-0125.1

Mekonnen, A., Thorncroft, C. D., & Aiyyer, A. R. (2006). Analysis of Convection and Its Association with African Easterly Waves. https://doi.org/10.1175/JCLI3920.1

Nowottnick, E. P., Rowe, A. K., Nehrir, A. R., Zawislak, J. A., Piña, A. J., McCarty, W., Barton-Grimley, R. A., Bedka, K. M., Bennett, J. R., Brammer, A., Buzanowicz, M. E., Chen, G., Chen, S.-H., Chen, S. S., Colarco, P. R., Cooney, J. W., Crosbie, E., Doyle, J., Fehr, T., … Zipser, E. J. (2024). Dust, Convection, Winds, and Waves: The 2022 NASA CPEX-CV Campaign. https://doi.org/10.1175/BAMS-D-23-0201.1

Núñez Ocasio, K. M. N., Evans, J. L., & Young, G. S. (2020). A Wave-Relative Framework Analysis of AEW–MCS Interactions Leading to Tropical Cyclogenesis. https://doi.org/10.1175/MWR-D-20-0152.1

Poveda, G., Mesa, O., Agudelo, P., Álvarez, J., Arias, P., Moreno, H., Salazar, L., Toro, V., & Vieira, S. (2002). INFLUENCIA DEL ENSO, OSCILACIÓN MADDEN-JULIAN, ONDAS DEL ESTE, HURACANES Y FASES DE LA LUNA EN EL CICLO DIURNO DE PRECIPITACIÓN EN LOS ANDES TROPICALES DE COLOMBIA.

Pytharoulis, I., & Thorncroft, C. (1999). The Low-Level Structure of African Easterly Waves in 1995. https://journals.ametsoc.org/view/journals/mwre/127/10/1520-0493_1999_127_2266_tllsoa_2.0.co_2.xml

Reed, R. J., Klinker, E., & Hollingsworth, A. (1988). The structure and characteristics of African easterly wave disturbances as determined from the ECMWF operational analysis/forecast system. Meteorology and Atmospheric Physics, 38(1), 22–33. https://doi.org/10.1007/BF01029944

Reed, R. J., Norquist, D. C., & Recker, E. E. (1977). The Structure and Properties of African Wave Disturbances as Observed During Phase III of GATE. https://journals.ametsoc.org/view/journals/mwre/105/3/1520-0493_1977_105_0317_tsapoa_2_0_co_2.xml

Russell, J. O. H., & Aiyyer, A. (2020). The Potential Vorticity Structure and Dynamics of African Easterly Waves. https://doi.org/10.1175/JAS-D-19-0019.1

Russell, J. O. H., Aiyyer, A., & Dylan White, J. (2020). African Easterly Wave Dynamics in Convection-Permitting Simulations: Rotational Stratiform Instability as a Conceptual Model. Journal of Advances in Modeling Earth Systems, 12(1), e2019MS001706. https://doi.org/10.1029/2019MS001706

Rydbeck, A. V., & Maloney, E. D. (2015). On the Convective Coupling and Moisture Organization of East Pacific Easterly Waves. https://doi.org/10.1175/JAS-D-15-0056.1

Schubert, W. H., Ciesielski, P. E., Stevens, D. E., & Kuo, H.-C. (1991). Potential Vorticity Modeling of the ITCZ and the Hadley Circulation. https://journals.ametsoc.org/view/journals/atsc/48/12/1520-0469_1991_048_1493_pvmoti_2_0_co_2.xml

Schwendike, J., & Jones, S. C. (2010). Convection in an African Easterly Wave over West Africa and the eastern Atlantic: A model case study of Helene (2006). Quarterly Journal of the Royal Meteorological Society, 136(S1), 364–396. https://doi.org/10.1002/qj.566

Semunegus, H., Mekonnen, A., & Schreck III, C. J. (2017). Characterization of convective systems and their association with African easterly waves. International Journal of Climatology, 37(12), 4486–4492. https://doi.org/10.1002/joc.5085

Snyder, A. D., Pu, Z., & Zhu, Y. (2010). Tracking and Verification of East Atlantic Tropical Cyclone Genesis in the NCEP Global Ensemble: Case Studies during the NASA African Monsoon Multidisciplinary Analyses. https://doi.org/10.1175/2010WAF2222332.1

Thompson, R. M., Payne, S. W., Recker, E. E., & Reed, R. J. (1979). Structure and Properties of Synoptic-Scale Wave Disturbances in the Intertropical Convergence Zone of the Eastern Atlantic. https://journals.ametsoc.org/view/journals/atsc/36/1/1520-0469_1979_036_0053_saposs_2_0_co_2.xml

Thorncroft, C., & Hodges, K. (2001). African Easterly Wave Variability and Its Relationship to Atlantic Tropical Cyclone Activity. Journal of Climate, 14(6), 1166–1179. https://doi.org/10.1175/1520-0442(2001)014<1166:AEWVAI>2.0.CO;2

Zawislak, J., & Zipser, E. J. (2010). Observations of Seven African Easterly Waves in the East Atlantic during 2006. https://doi.org/10.1175/2009JAS3118.1

Zawislak, J., & Zipser, E. J. (2014). Analysis of the Thermodynamic Properties of Developing and Nondeveloping Tropical Disturbances Using a Comprehensive Dropsonde Dataset. Monthly Weather Review, 142(3), 1250–1264. https://doi.org/10.1175/MWR-D-13-00253.1

Zawislak, Jon, Edward Nowottnick, and Amin Nehrir. 2022. Convective Processes Experiment – Cabo Verde (CPEX-CV) Field Campaign Collection [indicate subset used]. Data available

online from the NASA EOSDIS Global Hydrometeorology Resource Center Distributed Active Archive Center, Huntsville, Alabama, U.S.A. doi: http://dx.doi.org/10.5067/CPEXCV/DATA101